

# AUTOMATED OPTIMAL SYNTHESIS OF MICROACCELEROMETERS

Tamal Mukherjee<sup>†</sup>, Yong Zhou<sup>†</sup>, and Gary K. Fedder<sup>†\*</sup>

<sup>†</sup>Department of Electrical and Computer Engineering and <sup>\*</sup>The Robotics Institute  
Carnegie Mellon University  
Pittsburgh, PA, 15213-3890

## ABSTRACT

The rapid layout synthesis of a lateral accelerometer from high-level functional specifications and design constraints is demonstrated. Functional parameters such as sensitivity, minimum and maximum detectable acceleration are satisfied while simultaneously optimizing a design objective, such as device area. The optimal synthesis tool allows exploration of micromechanical device and system design issues and objectives. Layout synthesis couples optimization-based design to determine the values of layout geometry followed with layout generation to translate the desired device performance into a device layout. This rapid layout generation allows for an ‘on-the-fly’ cell library generation methodology for use in design of integrated microsystems. In particular, the optimization-based approach to design allows the designer to determine the crucial design trade-offs in meeting the system-level performances, as shown by synthesis results presented.

**Keywords:** CAD, lateral accelerometer, synthesis

## INTRODUCTION

The advent of stable, VLSI-compatible MEMS fabrication technologies has led to the development of increasingly complex and integrated MEMS-based systems. Future systems are expected to contain hundreds or even thousands of mixed-domain devices. In particular, the miniaturization and batch-fabrication advantages of MEMS and electronics will enable the integration of a variety of sensing systems to achieve a sensing capability not previously possible in single devices. In these integrated systems, the main design decisions involve the system (*e.g.*, how many accelerometers, their range of operation, how their raw data will be combined) rather than the device. Design of these integrated systems requires the use of CAD tools [1] to rapidly generate the design of each of the devices to be integrated into the system as well as to allow the system-level designer to understand the trade-offs inherent in system design for the application of interest.

For commonly used micromechanical device topologies, layout synthesis provides an automated mechanism for generating valid layout given high-level design specifications and constraints as input. Due to the tight coupling between form and function in mechanical systems, MEMS design effectively involves both parametric design and layout design. Parametric design involves determining the values of the design parameters such that the device meets its performance requirements. Layout generation involves the physical design of the masks used to fabricate the design. Optimization has been used for spring/active area trade-offs [2], and for comb drives [3]. MEMS device layout generators such as [4][5] have focused on direct layout generation from physical definitions similar to module generators in VLSI microelectronics. The design problem is modeled as a

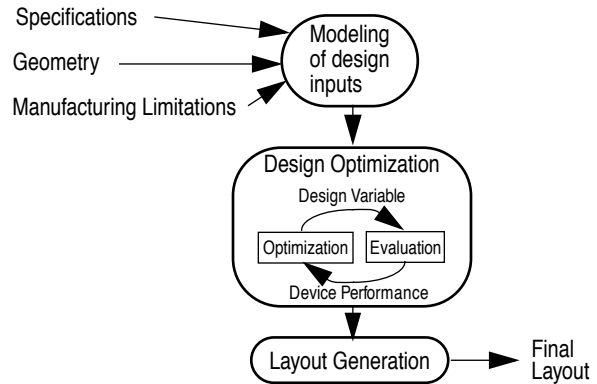


Figure 1: Steps in the synthesis process

formal numerical optimization problem, and then solved with powerful optimization techniques, resulting in a tool that automates the design synthesis of MEMS structures. Furthermore, the functional model of the device and its geometrical layout model are tightly integrated, to aid in the generation of the layout parameters that completely describe the layout [6]. The process of modeling the design problem involves determining the design variables, the numerical design constraints, and the quantitative design objective. The resulting optimal synthesis tool enforces codification of all relevant variables and constraints and allows rapid exploration of micromechanical design issues and objectives.

The lateral accelerometer topology in this study has been thoroughly analyzed [7][8][9][10] and is commonly found in commercial inertial sensors [11]. This flexible topology is the seed to a variety of accelerometers of different performances, and therefore represents a good topology for synthesis. The MUMPs process and design rules is used to constrain the design space [12]. This synthesis methodology can be easily extended to alternate processes (*e.g.*, iMEMS [13] and CMOS-MEMS [14]) where the same lateral accelerometer topology has been designed (*i.e.*, the ADXL family [11] and an integrated lateral capacitive CMOS accelerometer [15]).

Lumped-parameter electromechanical models with three degrees-of-freedom (in plane  $x$ ,  $y$  and  $\theta$ ) have been derived to link the physical and behavioral parameters of the accelerometer. These models provide the evaluation capability required for doing design, as shown in Figure 1. The optimization-based design process iterates on the values of the design variables until the evaluation module indicates that the design specifications are met for the set of process/operating parameters.

## MICROACCELEROMETER DESCRIPTION

The MUMPs technology chosen for this synthesis work is well documented [12]. Accelerometer structures are formed from a 2  $\mu\text{m}$ -thick layer of polysilicon deposited over a 2  $\mu\text{m}$ -thick sacrificial spacer layer of phosphosilicate glass (PSG). The

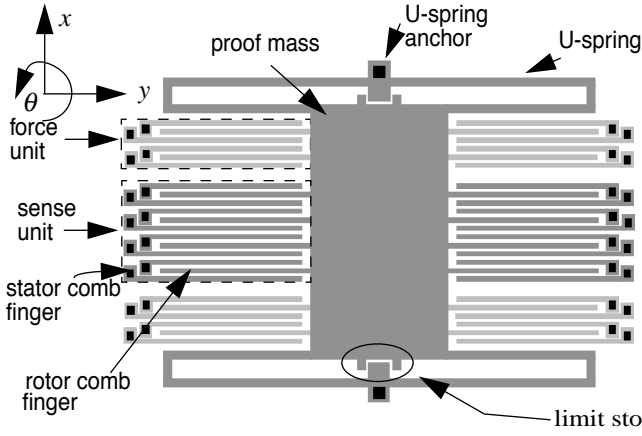


Figure 2: Layout of the lateral capacitive microaccelerometer. The black areas indicate the anchors between the polysilicon structure and the bottom layer. The rest of the structure is suspended  $2 \mu\text{m}$  above the bottom layer. The force units are shown in a lighter shade than the rest of the structure.

PSG contact cuts act as mechanical anchor points that fix the microstructure to the substrate surface after the final HF release etch is completed.

The accelerometer consists of a movable proof mass, suspended by two U-shape spring beams on both sides, as shown in Figure 2. External acceleration causes the proof mass to move relative to the substrate, subject to restoring spring forces and the damping provided by the motion of air around the device as shown in Figure 3. The suspension is designed to be compliant in the  $x$  direction of motion and to be stiff in the orthogonal direction ( $y$ ) to keep the comb fingers aligned. Movable comb (rotor) fingers are attached to the proof mass. They are combined with the fixed comb (stator) fingers to form the sensing and force functional units. The applied voltages on the force unit causes a net electrostatic force to pull the proof mass in the desired direction. These force fingers can be used for either self-test or force-feedback control. The sensing fingers form a capacitive bridge, which is modulated with voltage  $V_m$  during sensing. The divider output is proportional to the difference in the capacitances, and therefore to the proof mass position. This divider voltage passes through a buffer (Figure 4) and is then demodulated (not shown) to generate the final output voltage. At two ends of the proof mass there are four small rectangular cantilever beams, which act as limit stops on the  $x$  and  $y$  displacement to prevent contact between rotor and stator fingers.

Design variables of the microaccelerometer include the comb drive voltage, the numbers of fingers for the sense and force units and fourteen structural parameters as detailed in Figure 5. This figure shows a generic differential comb drive. The number of fingers for the force ( $N_f$ ) and sense ( $N_s$ ) units are independent,

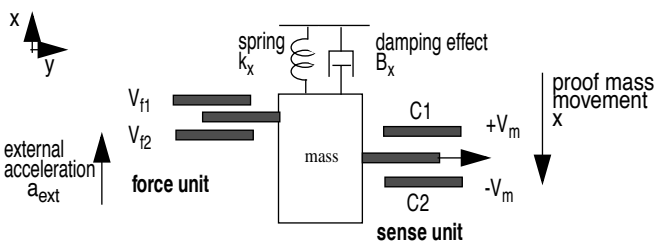


Figure 3: Schematic of an capacitive accelerometer

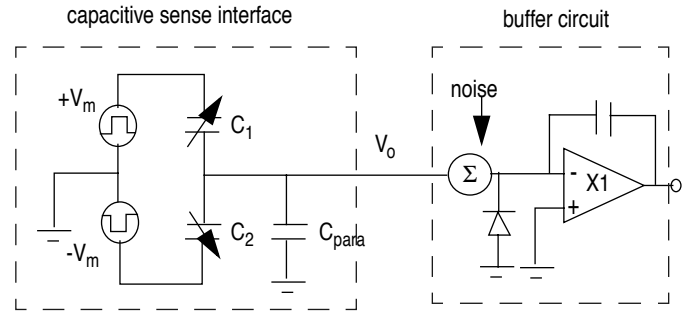


Figure 4: Accelerometer sensing interface.

as is the finger gaps ( $g_f$  and  $g_s$ ) in each unit. The finger lengths ( $L_f$ ), widths ( $W_f$ ) and overlaps ( $X_0$ ) for the two units are however set to be identical to take advantage of symmetry for minimizing manufacturing variations. The U-spring is modeled using the lengths of the two beams ( $L_{b1}$  and  $L_{b2}$ ) which have a common width ( $W_b$ ) and the truss geometry ( $L_t$  and  $W_t$ ). The mass geometry ( $L_{pm}$  and  $W_{pm}$ ) and the limit-stop gaps ( $g_{x,limit}$  and  $g_{y,limit}$ ) round up the list of design variables. Several geometric variables, such as length and width of the anchors in the comb drive are necessary to completely define the layout but do not affect accelerometer behavior. These variables are labelled ‘style’ parameters because they affect the stylistic look of the device rather than the device performance. For this work, ten style variables for the accelerometer were identified [16].

The accelerometer is modeled as a mechanical system under external acceleration ( $m_x \ddot{x} + B_x \dot{x} + k_x x = F_{ext} = ma_{ext}$  for the  $x$  direction) followed by a capacitive transducer. Off-axis translational and rotational modes ( $y$  and  $\theta$  directions) are also modeled to ensure that the final design moves only in the primary ( $x$ ) direction. The out-of-plane modes and other higher order modes are not included in the present synthesis implementation. The effect of spring mass on resonance frequency is incorporated in effective masses for each lateral mode. The maximum velocity and total kinetic energy of the spring, from which the effective mass is extracted, is approximated from static mode shapes. Viscous damping generated by the moving proof mass in air [8] is modeled as Couette-flow damping below the accelerometer [17], Stokes flow above the accelerometer [9], and squeeze-film damping between the comb fingers. The effect of etch holes [18] on lateral damping is not included. Damping factors of the other

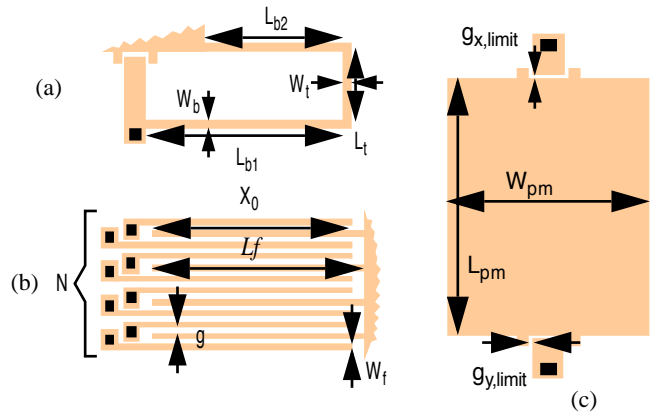


Figure 5: Parametrized elements of the accelerometer. (a) U-spring, (b) comb drive, (c) proof mass and anchor

lateral modes do not enter into the design constraints, so only  $B_x$  is calculated. Linear equations for the U-spring constants are found by using energy methods to solve for displacement under unit load on the end of the spring [19]. Mode coupling due to mismatches in spring geometry during manufacturing can lead to cross-axis sensitivity. Therefore models for the coupling spring constant ( $k_{xy}$ ) are also derived in addition to the self spring constants ( $k_x$ ,  $k_y$ , and  $k_\theta$ ). The electrostatic force generated by the modulation voltage across the sense fingers or the drive voltage on the force fingers can be derived as a function of finger width, gap, structure thickness, and sacrificial spacer thickness as in [20]. The sense unit exhibits electrostatic spring softening, which can be obtained by differentiating the electrostatic force by the lateral displacement. This spring term is included in series with the mechanical stiffness term in the  $x$  direction. These models are general mechanical models for any device with the layout topology of Figure 2, and form the starting point for models of the design constraints described in the next section.

## LAYOUT SYNTHESIS

### Design Constraints

Constraints on the design specifications are assigned realistic values for synthesizing a valid accelerometer. Alternative constraint values can be readily assigned in the implementation. The accelerometer behavior is different for open-loop operation compared to closed-loop operation. We initially describe the open-loop behavior.

Accelerometer sensitivity is defined as the ratio of output voltage over the input acceleration. Combining second-order mechanical system analysis and the algebraic voltage division from the single-ended half-bridge capacitive sense circuit of Figure 4, we see  $S = V_o/a_{ext} = 2m_x C_0/k_x g_0(2C_0 + C_{para})V_m$ , where  $C_0$  is the finger capacitance and  $g_0$  is the finger gap when there is no acceleration (*i.e.*,  $C_1=C_2=C_0$ ). Further electronic gain can be added after the unity-gain buffer if needed [8][11], but is ignored in this work. Currently  $C_{para}$  is specified by the designer, however, a combined accelerometer/buffer synthesis system can automatically design and extract  $C_{para}$  if necessary.

The minimum detectable acceleration is determined by the total input-referred noise of the accelerometer, and is governed by the Brownian (thermomechanical) noise due to random collisions between the proof mass and the air molecules and by the electronic noise from the front-end buffer circuit. Given a designer-specified electronic noise,  $v_{n-ckt}$ , we can compute the total noise, and therefore the minimum detectable acceleration

( $a_{min}$ ) by  $a_{min} = \sqrt{(v_{n-ckt}/S)^2 + a_{n-B}^2}$  where  $S$  is the accelerometer sensitivity ( $V_o/a_{ext}$ ). The Brownian noise is obtained from

$\sqrt{a_{n-B}^2} = \sqrt{4k_B T \omega_r / m Q} \sqrt{\Delta f}$  where  $k_B$  is Boltzman's constant,  $T$  is the temperature,  $\omega_r$  is the resonant frequency of the accelerometer,  $m$  is the effective mass of the accelerometer,  $Q$  is the quality factor and  $\Delta f$  is the range of frequencies for the input acceleration as in [7].

In open-loop operation, a parallel-plate instability occurs because the increase in mechanical restoring force is slower than

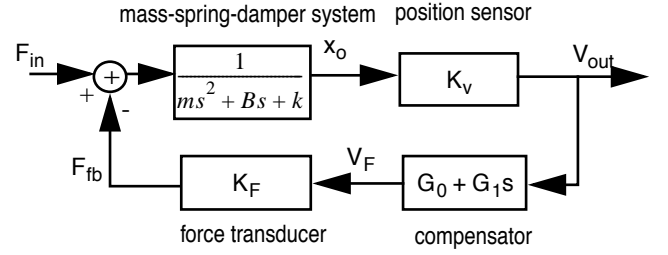


Figure 6: Analog feedback loop.

the increase in electrostatic force beyond the snap-in point. If the acceleration is large enough to move the rotor fingers beyond this point, the proof mass will snap into the limit stop. At equilibrium, the restoring spring force is equal to the sum of the inertial force and the electrostatic force. Solving this for acceleration as a function of comb finger displacement leads to  $a(x) = (k_x x (g_0^2 - x^2)^2 - 2C_0 V_m^2 g_0^2 x) / (m_x (g_0^2 - x^2)^2)$ . The maximum displacement from this equation is the snap-in point  $x_{snap}$ , which occurs for accelerations larger than  $a_{snap}$ , as related by the above equation. Accelerations larger than  $a_{snap}$  cannot be detected. The limit gap  $g_{x,limit}$  is set by the maximum expected displacement, obtained by inverting the above equation  $a(x_{max}) = a_{max}$  to solve for  $x_{max}$ .

Finite cross-axis sensitivity arises from the misalignment of the package orientation [11] or from process variations (for example, the mismatch in the etch wall of the spring beam and truss [10]). As package misalignment cannot be synthesized, this work only considers process variations. Under perfect matching, layout symmetry ensures that the  $x$  displacement, hence  $V_o$ , is not affected by acceleration in both  $y$  and  $z$  directions. However, if there is a mismatch in the four U-springs, a  $y$ -directed acceleration will cause the proof mass to be displaced in the  $x$  direction, leading to undesired mode coupling. The spring mismatch can be characterized as  $k_{xy}$ . Without process variations,  $k_{xy} = \infty$ , thus there is no cross-axis sensitivity. The cross-axis sensitivity is the ratio of the output voltage due to off-axis acceleration to same-axis acceleration,  $S_{cr} = (k_{xx}/m_x)/(k_{xy}/m_y)$ .

A proportional-derivative compensator is used for closed-loop operation as shown in Figure 6. Solving the transfer function to obtain the final value provides the steady-state displacement,  $x_{o,steady}$ . If the maximum expected open-loop displacement due to  $a_{max}$  (*i.e.*,  $x_{max}$ ) is less than the open-loop snap-in point,  $x_{snap}$ , snap-in will not occur, so  $x_{o,steady}$  is set to  $x_{max}$ . The dc transfer function reduces to the open-loop case, and the feedback tunes the transient response only. If  $x_{max} > x_{snap}$ , then  $x_{o,steady}$  is set to  $x_{snap}$  to prevent snap-in. This critically damped closed-loop system increases the maximum detectable acceleration in two ways: it eliminates displacement ringing and also provides a steady-state feedback force when a large input acceleration is applied.

In closed-loop feedback, the sensitivity equation (obtained from the transfer function analysis in the steady state) is  $V_o/a_{in}|_{closed} = m_x K_V / (K_F K_V G_0 + k_x) = K_V x_{o,steady} a_{max}$ . This reduces to the open-loop case when  $x_{o,steady} < x_{snap}$ .

The maximum detectable acceleration in closed-loop is derived from the closed-loop transfer function to be  $a_{max} = V_{F,p} \alpha^2 / (K_V(G_0 - G_0 e^{-\alpha t_p} - \alpha(G_0 - \alpha G_1)t_p e^{-\alpha t_p}))$ , where  $\alpha = (B + G_1 K_F K_V) / 2m$  and  $t_p = G_1 / (\alpha G_1 - G_0)$  is the time at which the peak value of feedback voltage (*viz.*,  $V_{F,p}$ ) occurs. The remaining equations of accelerometer function are unchanged from the open-loop case.

The layout is constrained by the MUMPs design rules. Technology-driven design rules set minimum beam widths and minimum spaces between structures. Maximum element lengths are constrained to 400  $\mu\text{m}$  to avoid problems with undesirable curling due to stress gradients in the structural film and possible sticking and breakage during the wet release etch. Additional manufacturability constraints such as buckling are added in the form of [6]. The remaining design constraints ensure that the derived accelerometer behavioral equations remain accurate such as limits on spring softening, self-test force, and mode separation.

The final set of constraints include geometrical constraints that arise from the layout topology of the accelerometer. They are necessary for a physically valid design. Examples of such constraints include the relationship between the sense and force unit gaps ( $g_s$  and  $g_f$ ) and the limit-stop gap ( $g_{x,limit}$ ).

## Synthesis Algorithm

Synthesis of the microaccelerometer will result in one of two possible outcomes. Several designs may satisfy the above constraints, or no designs may meet the constraints (null design space). The goal of synthesis is to select the design that minimizes an objective function and therefore may be considered optimal. The synthesized result depends very strongly on the choice of objective function. For the microaccelerometer, we have encoded three different objective functions to minimize: total active area, accelerometer noise, the normalized sum of area and noise and a fourth to maximize: the maximum detectable acceleration.

The enumeration of design constraints and objectives allows us to mathematically model the design problem as an optimization problem. The set of all acceptable designs is determined by the region in the design space where all the constraints are met: the *feasible* region. The design objective functions guide the optimization to the best design within the feasible region. This non-linear optimization problem can be solved using standard off-the-shelf solvers [21]. Evaluating the cost function involves using the lumped-element macromodels to determine the extent to which the design constraints are met, for the current values of the design variables. This cost function has multiple minima due to the complex non-linear characteristics of the individual equations in the lumped-element macromodel.

A gridded numerical optimization algorithm efficiently solves for the global minimum of the objective function. The use of a starting grid eliminates the need to provide good starting points to the gradient based optimization. This starting grid is obtained from a design-of-experiments style approach to partitioning the multivariate design space. Since some of the design variables are integer, a branch-and-bound approach to solving for the mixed integer and non-linear design variables is used.

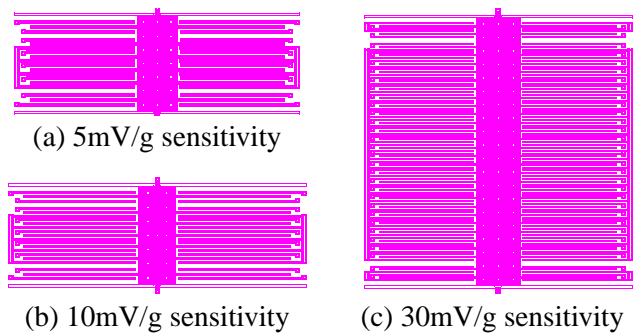


Figure 7: Synthesized minimal area and noise accelerometers

## RESULTS AND DISCUSSION

For visualization of the synthesis results, a parameterized module generator similar to the Consolidated Micromechanical Element Library (CaMEL) software [4] was used. It provides CIF output when given accelerometer layout parameters. Etch holes for the proof mass are used at 30  $\mu\text{m}$  intervals to ensure release.

Selected highlight results from the synthesis tool are presented below. These results share common specifications for the electronic noise in the buffer ( $v_{n-ckt}$ ) of 10nV/rtHz; the maximum area allowed of 700  $\mu\text{m}$  by 700  $\mu\text{m}$ ; the parasitic capacitance ( $C_{para}$ ) of 120fF; and the sense unit modulation voltage ( $V_m$ ) of 2.5V.

The first synthesis result considers the accelerometer under open-loop operation. One of the most important design metrics for an accelerometer is its noise performance. Minimizing the total acceleration noise inevitably leads to a large proof mass, which for surface-micromachined processes means large areas. Therefore, the first experiment minimizes the normalized combination of accelerometer area and noise, allowing trade-offs between these two performance metrics. Three accelerometers synthesized for different sensitivities, with noise < 0.1mg/rtHz and range > 10 g are shown in Figure 7. Increasing sensitivity requires increasing either or both the finger length or the number of fingers. Since the number of fingers is an integer variable, as we increase the specified sensitivity, the optimization chooses to first increase finger length (thereby reducing the proof mass width) until the noise-area trade-off allows it to increase the number of sense fingers. In particular, doubling the sensitivity from Figure 7(a) to (b) adds a comb finger, and increases the finger length from 250  $\mu\text{m}$  to 268  $\mu\text{m}$ . Further increases in sensitivity to 30mV/g leads to the addition of more than 20 comb fingers, with finger lengths reducing to 226  $\mu\text{m}$ . As the proof mass length increases, it effectively acts as if its a larger weight on the minimization of the accelerometer width, which explains the reduction in finger lengths. This example highlights the importance of selecting a design objective that best matches the desires of the designer. Once such an objective is chosen, the synthesis tool can be used to trade-off between the various design goals.

Synthesis enables a deeper understanding of the design space by allowing the designer to compare different topologies. Figure 8 compares the synthesized layouts of open-loop and a closed-loop accelerometer maximized for range (maximum detectable acceleration). In both cases, common specifications included a 20mV/g sensitivity, and noise < 0.1 mg/rtHz. In open-

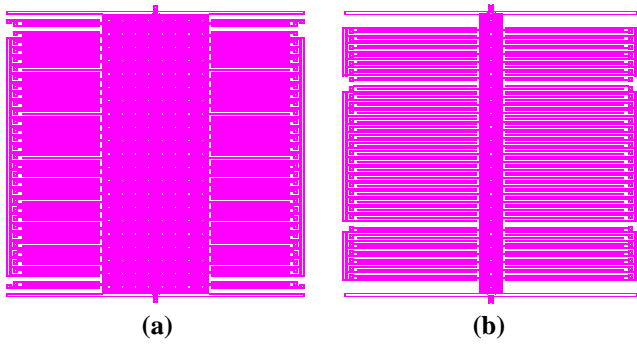


Figure 8: Synthesized layouts of (a) open-loop and (b) closed-loop accelerometers maximized for range.

loop, only a single force-unit finger is used for self-test. The force feedback helps increase the range from 21g to 151g. Increasing the number of feedback fingers requires that the sense-unit finger lengths increase to maintain the 20mV/g sensitivity specification, thereby reducing the proof mass width — the noise doubles, but is still within the specified engineering constraint.

Instead of a two-point comparison, a complete Pareto curve can be obtained, as shown in Figure 9. The curve was generated by minimizing noise for several fixed values of sensitivity, with range > 10g for all the designs. This curve allows the designer to determine the optimum device design from system constraints. As the required sensitivity increases, the number of sense fingers and the length of the fingers increases. Since the total accelerometer width is limited to 700 $\mu$ m, the increased finger length implies reduced proof mass width, which increases the total accelerometer noise. Since the designer tends to look for a high-sensitivity low-noise design, one option can be to use electronic buffers to boost sensitivity. Coupling the curve in Figure 9 with a gain-noise plot for a buffer can lead to the optimal system design.

In addition to manufacturing-oriented constraints such as buckling, used for all the synthesis runs, a cross-axis sensitivity specification was used to highlight the trade-off between noise and cross-axis sensitivity shown in Figure 10. Both the accelerometers were synthesized for 10g range and 5mV/g sensitivity.

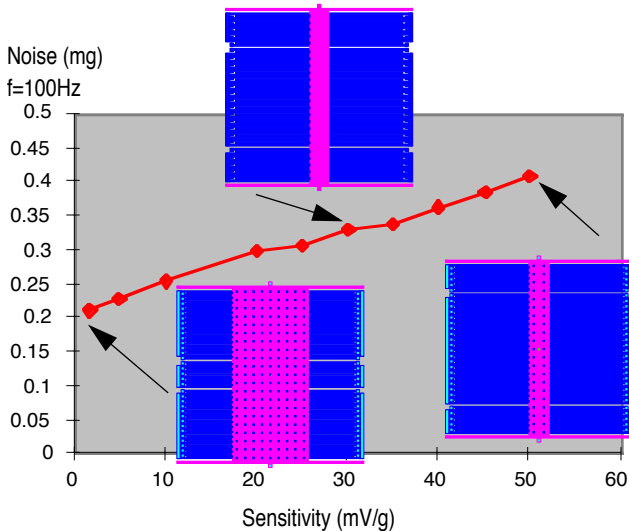


Figure 9: A Pareto curve showing the trade-off between sensitivity and noise.

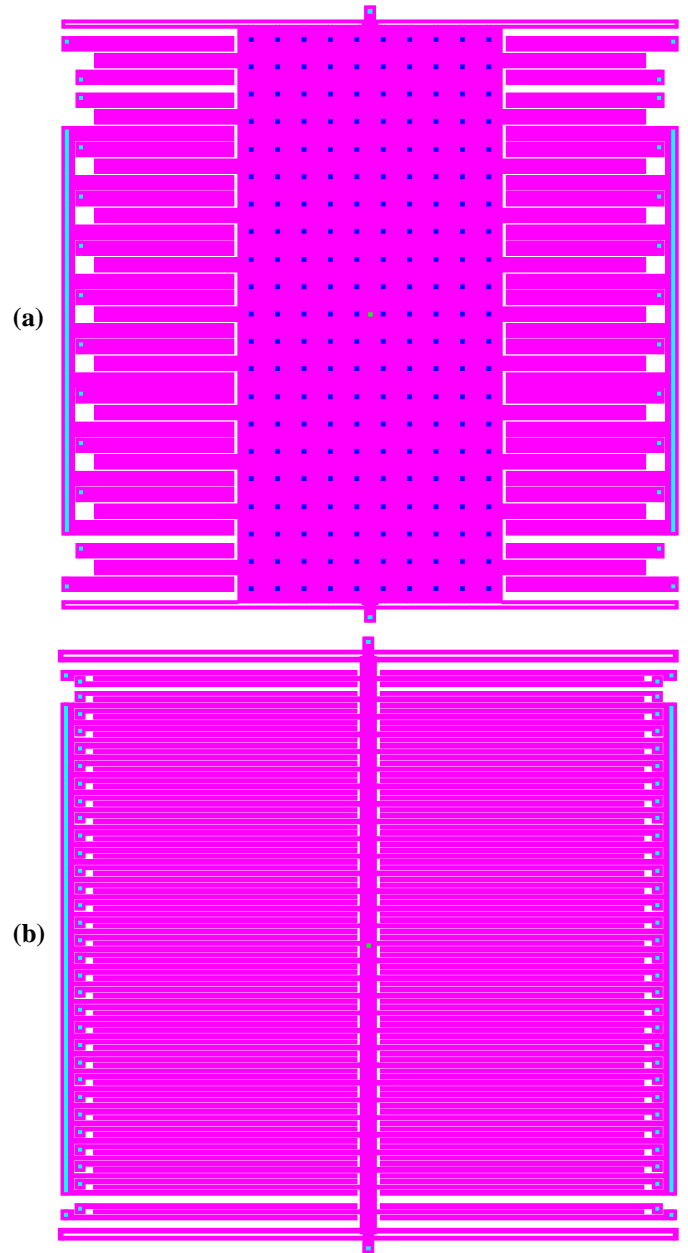


Figure 10: Synthesized layouts of (a) minimal noise and (b) minimal cross-axis sensitivity.

The noise increased from 18 $\mu$ g/rtHz to 54 $\mu$ g/rtHz, but the cross-axis sensitivity reduces from 0.27% to 0.004%. The proof mass width reached its maximum limit in Figure 10(a) and the fingers were fattened to further minimize noise. Cross-axis sensitivity arises due to tether beam width ( $W_b$ ) variations. The synthesis module accepts beam width variations (0.2 $\mu$ m was used for these results), and effectively increases beam widths to minimize the effect of the variation; in this case  $W_b$  increased from 2.95 $\mu$ m to 4.55 $\mu$ m. This increased tether beam width raises the cross-axis stiffness ( $k_{xy}$ ) by two orders of magnitude, thereby reducing cross-axis sensitivity. Since the self spring constant,  $k_x$ , is proportional to  $W_b^3$ , the beam lengths of the U-spring have to be increased to contain the increase in  $k_x$  (which affects both  $S_{cr}$  and  $S$ ). The geometric layout constraint that links the U-spring beam lengths with the proof mass width effectively forces the proof mass width to be minimized. In the end the spring constant

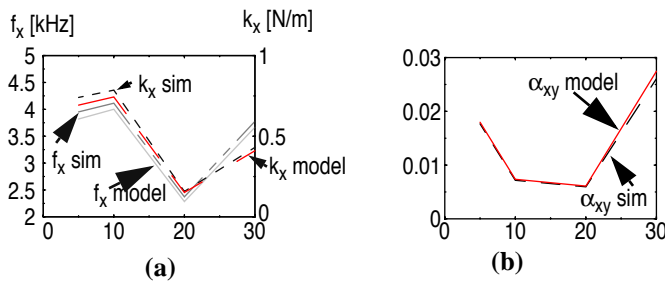


Figure 11: Comparison of predicted spring stiffness, resonant frequencies in the primary direction of motion (a). Predicted spring stiffness coupling between y and x mode (b).

$k_x$  increases from 0.7N/m to 1.3N/m, and mass decreases from 1.2 $\mu$ g to 0.48 $\mu$ g. The resulting increase in resonant frequency requires increasing  $C_0$  (by increasing the number of fingers) to maintain the desired sensitivity of 5mV/g.

The synthesis methodology uses lumped-parameter models for the effective spring constants and effective masses in the primary, off-axis, and coupling modes of the accelerometer. The accuracy of these lumped-parameter models for several synthesized accelerometers via finite-element analysis has been verified. Each synthesized accelerometer was modeled using 8-node plane stress element, to determine all in-plane stiffness and modes. Curves showing the comparison of the lumped-parameter models used in the synthesis and the finite-element models are shown in Figure 11. The curves are for the primary mode and the cross-axis mode, due to their use in the major engineering design specifications for the accelerometer. For the primary mode, the analytic stiffness and frequency models used in the synthesis are accurate to within 5% of finite-element simulation. For the cross-axis mode, the cross-axis stiffness arising from mismatch in the widths of the beams in the four U-springs has a 6% accuracy with respect to finite-element analysis.

## CONCLUSIONS

Synthesis algorithms have been successfully applied to automatic layout of surface-micromachined accelerometers. A prerequisite for synthesis is a set of lumped-parameter models that adequately link device behavior with physical design variables. One important benefit of creating synthesis tools is that it forces the codify of every design variable and design constraint which then becomes reusable information. Optimal synthesis enables exploration of the entire design space given specific user-specified constraints, as has been shown with the accelerometer example.

Once a mature structured design methodology is established for surface-micromachined MEMS, the synthesis techniques may be extended in the future to general parameterized designs.

## ACKNOWLEDGEMENT

The research effort was sponsored by DARPA/ETO F30602-96-2-0304, and in part by G. K. Fedder's NSF CAREER Award MIP-9625471.

## REFERENCES

[1] G. K. Fedder, "Structured Design of Integrated MEMS," *IEEE MEMS '99*, Orlando, FL, Jan 1999.  
 [2] D. Haronain, "Maximizing microelectromechanical sensor and actuator sensitivity by optimizing geometry," *Sensors and Actuators A*, 50(1995), pp. 223-236.

[3] W. Ye, S. Mukherjee, and N.C. MacDonald, "Optimal Shape Design of an Electrostatic Comb Drive in Microelectromechanical Systems", *J. Microelectromechanical System*, March 1998, vol. 7, pp. 16-26.  
 [4] *CaMEL Web Page*, <http://www.mcnc.org/camel.org>, MCNC MEMS Technology Applications Center, 3021 Cornwallis Road, Research Triangle Park, NC 27709.  
 [5] N. R. L. Lo, E. C. Berg, S. R. Quakkelaar, J. N. Simon, M. Tachiki, H.-J. Lee, and K. S. J. Pister, "Parametrized Layout Synthesis, Extraction, and SPICE Simulation for MEMS," *Proc. 1996 IEEE International Symposium on Circuits and Systems*, pp 481-484, Atlanta, GA, May 12-15, 1996.  
 [6] T. Mukherjee, S. Iyer, and G. K. Fedder, "Optimization-based Synthesis Of Microresonators," *Sensors and Actuators A*, October 1998, pp 118-127.  
 [7] B.E. Boser, R.T. Howe, "Surface micromachined accelerometers," *IEEE Custom Integrated Circuits Conf*, 1995, pp. 337-344.  
 [8] M. Lemkin and B. E. Boser, "A micromachined fully differential lateral accelerometer," *IEEE Custom Integrated Circuits Conf*, 1996, pp 315-318.  
 [9] Y.-H. Cho, A.P. Pisano and R.T. Howe, "Viscous damping model for laterally oscillating microstructures," *J. Microelectromechanical Systems*, vol. 3, (1994), pp. 81.  
 [10] N.R. Swart, S.F. Bart, M.H. Zaman, M. Mariappan, J.R. Gilbert, D. Murphy, "AutoMM: Automatic generation of dynamic macromodels for MEMS device", *Proc. IEEE MEMS '98*, Heidelberg, 1998, pp.178 -183.  
 [11] Analog Devices, "ADXL150 -  $\pm 50$  g accelerometer with 10 mg resolution", Datasheet, 1997, Norwood, MA 02062.  
 [12] D. A. Koester, R. Mahadevan, K. W. Markus, *MUMPS Introduction and Design Rules*, MCNC MEMS Technology Applications Center, 3021 Cornwallis Road, Research Triangle Park, NC 27709, rev. 3, Oct. 1994.  
 [13] *iMEMS Web Page*, <http://imems.mcnc.org/imems/imems.html>, Analog Devices/MCNC, Analog Devices, One Technology Way, Norwood, MA 02062.  
 [14] G. K. Fedder, S. Santhanam, M. L. Reed, S. C. Eagle, D. F. Guillou, M. S.-C. Lu, and L. R. Carley, "Laminated high-aspect-ratio structures in a conventional CMOS process," *Sensors and Actuators, A*, 57, pp. 103-110 (1996).  
 [15] G. Zhang, H. Xie, L. E. Derosset, and G. K. Fedder, "A Lateral Capacitive CMOS Accelerometer with Structural Curl Compensation," *IEEE MEMS '99*, Orlando, FL, Jan 1999.  
 [16] Y. Zhou, "Layout Synthesis of Accelerometers," M.S. Thesis, Carnegie Mellon University, Sep. 1998.  
 [17] X. Zhang, W. C. Tang, "Viscous Air Damping in Laterally Driven Microresonators", *Sensors and Materials*, V. 7, no. 6, 1995, pp.415- 430.  
 [18] N. Yazdi and K. Najafi, "An all-silicon single-wafer fabrication technology for precision microaccelerometers", *The 9th International Conference on Solid-State Sensors and Actuators - Transducers*, '97, Chicago, Illinois, June 1997, pp.1181- 4.  
 [19] J. M. Gere and S. P. Timoshenko, *Mechanics of Materials*, 4th ed., Boston: PWS Publishing Co., 1997.  
 [20] W. A. Johnson and L. K. Warne, *J. of Microelectromechanical Systems*, v.4, no.1, pp.49-59, 1995.  
 [21] P.E.Gill, W.Murry, M.A. Saunders and M.H. Wright, *User's Guide for NPSOL (Version 4.0): A Fortran Package for Nonlinear Programming*, Technical Report SOL 86-2, Stanford University, January 1986.